Electronic Supplementary Information

Solution-Processed Solar Cells Based on Inorganic Bulk Heterojunctions with Evident Hole Contribution to Photocurrent Generation

Zeliang Qiu,[a] Changwen Liu,[a] Guoxing Pan,[b] Weili Meng,[a] Wenjin Yue,[a] Junwei Chen,[a] Xun Zhou,[a] Fapei Zhang,[b] Mingtai Wang[a,*]

[a]*Institute of Plasma Physics, Chinese Academy of Sciences, Hefei 230031, P. R. China*
[b]*High Magnetic Field Laboratory, Chinese Academy of Sciences, Hefei 230031, P. R. China*

[*]Corresponding author. Tel./Fax: 0086-551-65593171; Email address: mtwang@ipp.ac.cn

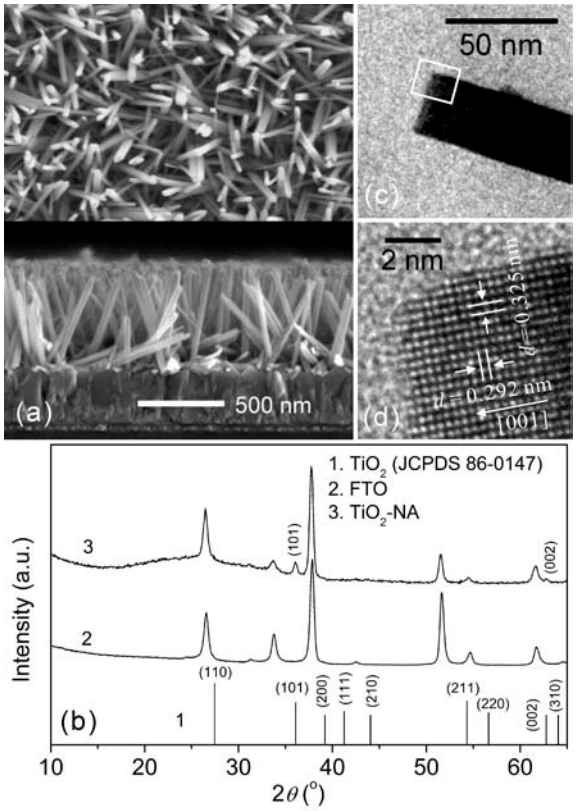

Figure S1. Characterization of the TiO_2-NA grown on FTO glass sheet. (a) SEM, (b) XRD, (c) TEM and (d) HRTEM. The HRTEM image in (d) was taken from the marked region on the TEM image in (c).

Notes to Figure S1: The nanorods have a length of ca. 600 nm and a diameter of 40–50 nm. The XRD diffraction peaks of the TiO_2-NA match well rutile TiO_2 (JCPDS #86–0147, $a = b = 4.594$ Å and $c = 2.959$ Å). The HRTEM image of the TiO_2 nanorod (d) exhibits two-dimensional lattice structures, and the lattice fringes with interplanar spacings of $d = 0.292$ nm and $d = 0.325$ nm are clearly imaged, which match the spacing distances of (001) ($d = 0.29586$ nm) and (110) ($d = 0.32484$ nm) crystal planes of rutile TiO_2, respectively. The lattice fringes of (001) planes are perpendicular to the growth direction, confirming that the TiO_2 nanorods in TiO_2-NA grow along [001] direction.[1]

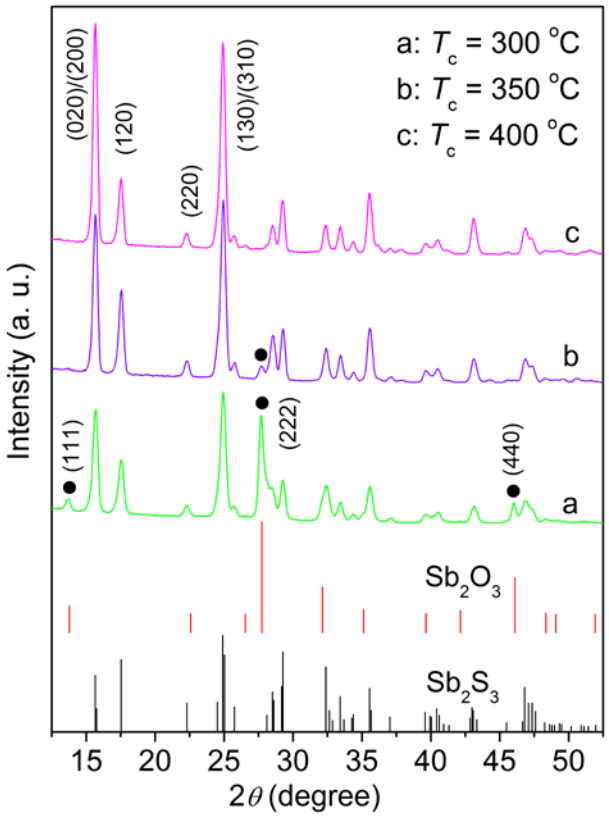

Figure S2. XRD patterns of differently crystallized Sb_2S_3/TiO_2-BHJs. (a) T_c = 300 °C, (b) T_c = 350 °C and (c) T_c = 400 °C. The XRD pattern for Sb_2S_3 is based on the data of orthorhombic Sb_2S_3 (stibnite) (JCPDS card 42-1393); the ● marks identify the diffraction peaks for Sb_2O_3 (Senarmontite, JCPDS card 72-1334).

Notes to Figure S2: The TiO_2-NA diffraction peaks are not observed when Sb_2S_3 is present, because it is covered by a thicker Sb_2S_3 layer. In the Sb_2S_3/TiO_2-BHJs with T_c = 300 °C, we observed the considerably intensive diffraction peaks for Sb_2O_3 (Senarmontite). However, increasing T_c to 350 °C, the diffraction peaks for Sb_2O_3 gets significantly reduced. As T_c is increased to 400 °C, almost not Sb_2O_3 is evident by XRD. Similarly, the presence of Sb_2O_3 was also observed in the Sb_2S_3 thermally annealed at 330 °C for 30 min in Ar atmosphere.[2] Some authors think that Sb_2S_3 is oxidized into Sb_2S_3 as it is exposed to air.[3] Note that the crystallized Sb_2S_3/TiO_2-BHJs samples were kept in N_2 atmosphere before XRD measurements; we let the samples be exposed to air for about 24 h after the first XRD measurements, the re-examination of the samples by XRD did not show any evident change in the diffraction peak intensity of Sb_2O_3, indicating that the oxidation of Sb_2S_3 takes place during the annealing process.[4] Clearly, our XRD data show that increasing T_c from 300 to 400 °C reduces greatly the oxidation of Sb_2S_3, but enhances significantly the Sb_2S_3 crystallinity in Sb_2S_3/TiO_2-BHJs.

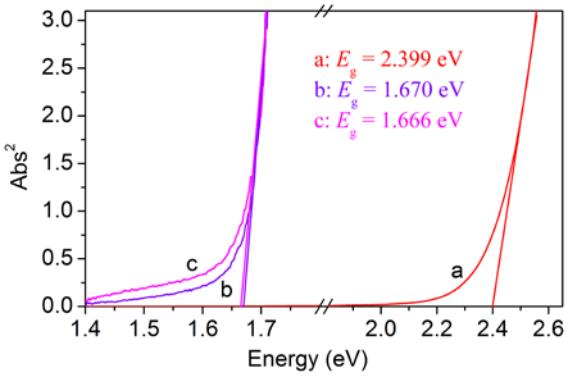

Figure S3. Direct optical band gaps of the Sb_2S_3 layers in Sb_2S_3/TiO_2-BHJs. (a) as-deposited, (b) T_c = 350 °C and (c) T_c = 400 °C. The band gaps is approximated using the direct band gap method, by plotting the squared absorbance versus energy and extrapolating to zero.

Notes to Figure S3: Since the difference between the band gaps for the samples with T_c = 350 and 400 °C is quite small (<< 5%), the two samples have almost the same band-gap when considering the experimental errors; we take the averaged band gap of 1.67 eV for both samples for simplicity.

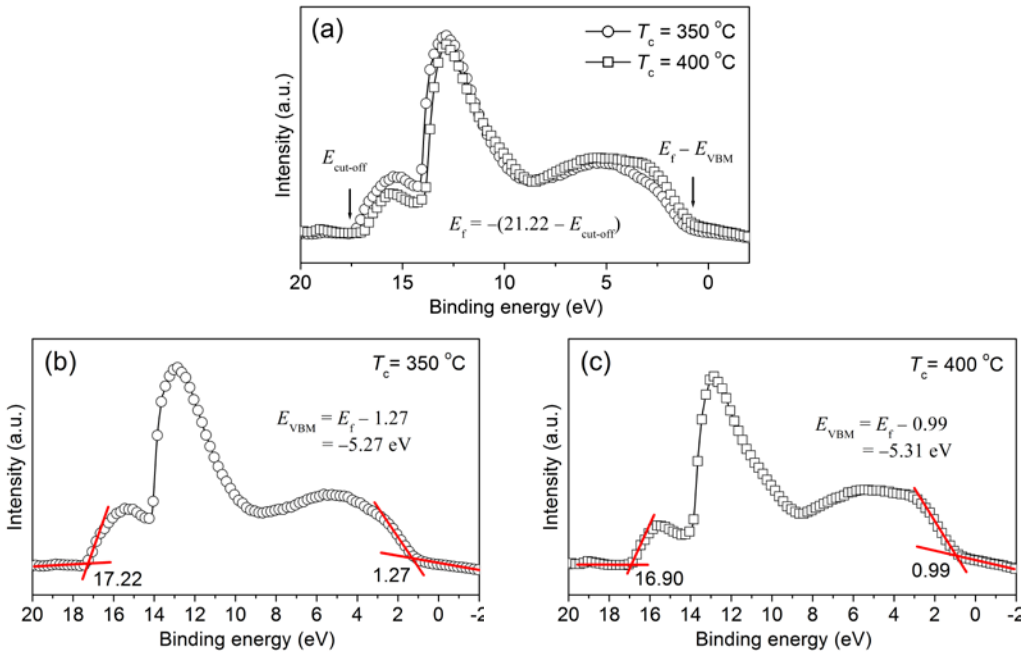

Figure S4. UPS spectra of the Sb_2S_3 layers in the Sb_2S_3/TiO_2-BHJs crystallized at 350 °C and 400 °C. (a) Comparison between the UPS spectra of samples. (b, c) Determination of the valence band maximum energy (E_{VBM}) values.

Notes to Figure S4: UPS was used to determine the Fermi level (E_f) and the valence band maximum (E_{VBM}) with respect to vacuum level of the Sb_2S_3 layers subjected to different crystallization temperatures (T_c).[5,6] The cut-off binding energy ($E_{cut-off}$) is determined by the intercept of the linear portion of the spectrum (high binding energy edge) with baseline, the difference between E_f and E_{VBM} is determined by the intersection of the linear portion of the spectra with the baseline in the low binding energy region. Accordingly, the E_{VBM} values for the Sb_2S_3 layers with T_c = 350 and 400 °C were

obtained to be −5.27 eV and −5.31 eV, respectively. The conduction band minimum (E_{CBM}) values for the samples are further calculated by adding the corresponding optical band-gap (Figure S3) to E_{VBM}, that is, E_{CBM} = −3.60 eV (for T_c = 350 °C) and −3.65 eV (for T_c = 400 °C). These results are comparable to the values of Sb_2S_3 reported in the literature.[7] The difference between the E_{VBM} (or E_{CBM}) energy levels for T_c = 350 and 400 °C is rather small (<< 5%) and may be due to the experimental errors, we take the averaged E_{VBM} of −5.29 eV and E_{CBM} of −3.63 eV for both samples for simplicity.

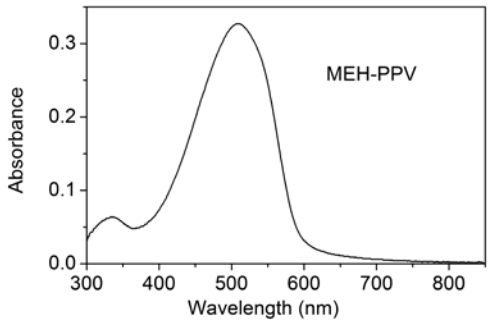

Figure S5. Absorption spectrum of MEH-PPV films on quartz substrates. MEH-PPV film exhibits an absorption band in 400–600 nm due to π–π* transition with the absorption maximum at 510 nm.

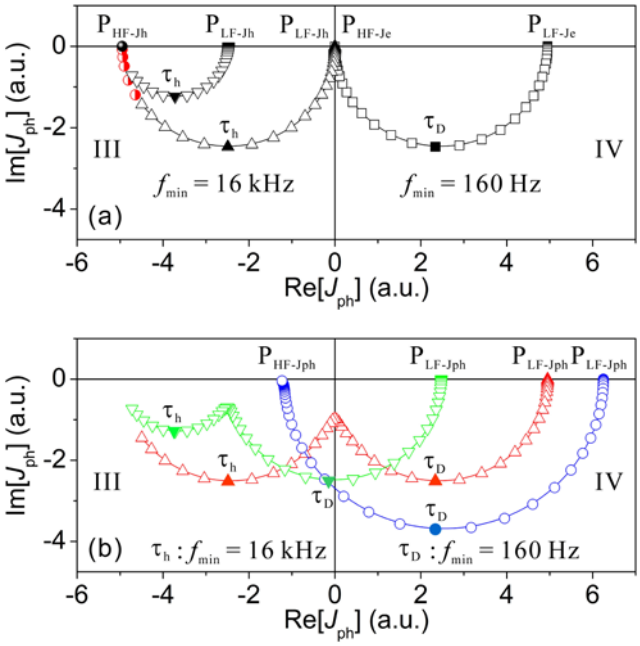

Figure S6. IMPS spectra calculated from eq 3 in the main text with $\tau_D = 10^{-3}$ s, $\tau_h = 10^{-5}$ s, ω = 0.01 Hz– 50 kHz (a–b) except for ω = 0.01 Hz – 10 MHz for the (◑) dots in plot (a). Other calculation parameters are: (a) (□) G_e = 4.95 and G_h = 0; (△,◑) G_h = 4.95, β_h = 1 and G_e = 0; (▽) G_h = 4.95, β_h = 0.5 and G_e = 0; (●) G_h = 4.95, β_h = 0 and G_e = 0. (b) (△) $G_e = -G_h$ = 4.95, and β_h = 1; (▽) $G_e = -G_h$ = 4.95, β_h = 1/2; (○) G_e = 4.95×1.5, G_h = −4.95/4, and β_h = 1/20. The solid symbols identify the time constants f_{min} values for electrons and holes; crossing points P_{HF} and P_{LF} have the frequencies of 8 MHz and 1 Hz, respectively.

Notes to Figure S6: This figure shows the dependence of the calculated IMPS shape ($J_{ph} = J_e + J_h$) on the parameters G_e and β_h, where $J_e = G_e/(1 + i\omega\tau_D)$ and $J_h = G_h[1 - \beta_h/(1 + i\omega\tau_h)]$. For convenience, the crossing points of IMPS response with the real axis at high and low frequency are referred to as P_{HF} and P_{LF}, respectively; we also use "Jh", "Je" and "Jph" in subscripts to distinguish the kinds of the crossing

points. Due to the serious trapping and fast recombination of holes in Sb_2S_3,[8,9] τ_h is set to be two orders of magnitude lower than τ_D for calculation.

(1) IMPS response for J_e (Figure S6a): The simulated IMPS response for J_e shows one distorted semicircle in the fourth quadrant of complex plane due to the electron transport for no J_h contribution (i.e., G_h = 0), where the value of crossing point $P_{LF\text{-}Je}$ is G_e, i.e., the J_e under steady-state condition.

(2) IMPS response for J_h (Figure S6a): The simulated IMPS response for J_h shows one distorted semicircle in the third quadrant of complex plane due to the trapped hole relaxation for no J_e contribution (i.e., G_e = 0); as the modulation frequency is rather high, the IMPS response for J_h will cross the real axis at $P_{HF\text{-}Jh}$ with a value of G_h meaning a maximal J_h limit when the relaxation loss is absent; moreover, the crossing point $P_{LF\text{-}Jh}$ value is the J_h under steady-state condition and strongly correlates with the parameter β_h, and a smaller β_h for a certain G_h makes the $P_{LF\text{-}Jh}$ approaching $P_{HF\text{-}Jh}$ in position.

(3) IMPS response for J_{ph} (Figure S6b): When both J_h and J_e are present, two semicircles can be obtained, in which the value of crossing point $P_{LF\text{-}Jph}$ is J_{ph} (i.e., = $J_e + J_h = G_e + J_h$) that is the steady-state photocurrent limit determining the efficiency in practical devices, while the $P_{HF\text{-}Jph}$ may not appear when the modulation frequency is not high enough. Given appropriate G_e, G_h and β_h, one can get the IMPS response in a form of a single semicircle with the time constant dominated by the electron transport in the IV quadrant and the indiscernible semicircle for J_h (or the time constant for hole relaxation) in the III quadrant in agreement with experimental observations (Figure 7b in the main text), in which the crossing point $P_{HF\text{-}Jph}$ has the value of G_h. Therefore, the IMPS responses going from the IV into III quadrant of complex plane is reasonably a strong indication of the contribution to photocurrent generation from the photogenerated holes in Sb_2S_3 layer. Note, whether the semicircle for J_h in IMPS response is discernible depends significantly on β_h and the G_h relative to G_e; in practice, the reduction in β_h for the hole trapping degree should also reduce the charge recombination and bring forth the increase in both G_e and G_h.

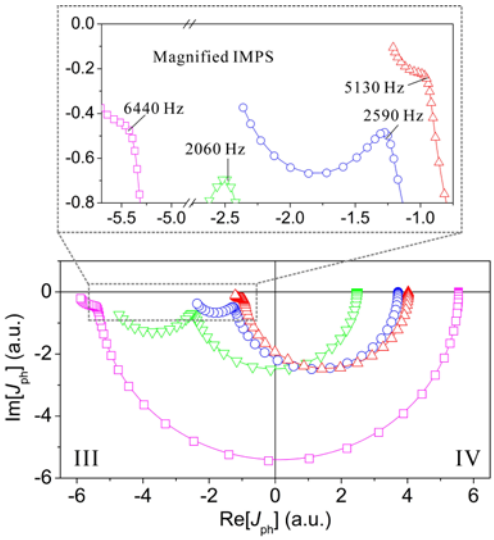

Figure S7. IMPS spectra calculated by eq 3 in the main text with $\tau_D = 10^{-3}$ s, $\tau_h = 10^{-5}$ s, ω = 0.01 Hz – 50 kHz. Other calculation parameters are: (▽) G_e = 4.95, G_h = –4.95, β_h = 1/2; (○) G_e = 4.95, G_h = –4.95/2, and β_h = 1/2; (△) G_e = 4.95, G_h = –4.95/4 and β_h = 1/4; (□) G_e = 4.95×2.2, G_h = –4.95×1.2, β_h = 1/10. **Note**, the magnified high frequency region is used to identify that the frequency of the turning point for the process change from electron transport to hole relaxation is not unchanged, but strongly depends on the G_e, G_h and β_h values.

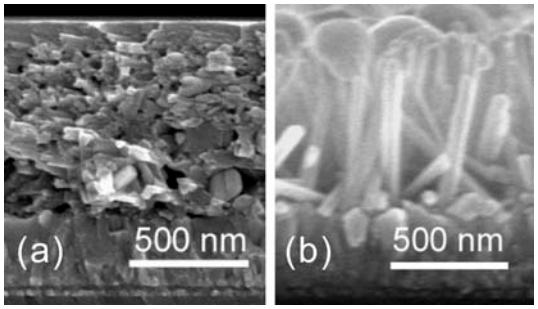

Figure S8. Sectional SEM image of Sb_2S_3/TiO_2-BHJs crystallized at 300 °C (a) and 450 °C (b).

Notes to Figure S8: The XRD data showed that the annealing at 300 °C results in a much lower Sb_2S_3 crystallinity in Sb_2S_3/TiO_2-BHJs film with respect to samples crystallized at 350 and 400 °C (Figure S2). SEM image revealed that Sb_2S_3/TiO_2-BHJs with T_c = 300 °C still exhibits a nanomorphology with the enlarged nanoparticles inside the Sb_2S_3 layer, which is similar to the morphology in the as-deposited Sb_2S_3/TiO_2-BHJs film, but quite different from the formation of a crystallized and continuous Sb_2S_3 layer with large grains around TiO_2 nanorods for T_c = 350–400 °C. However, SEM results show that thermal annealing at 450 °C removes the major part of Sb_2S_3 from TiO_2-NA. The removal of Sb_2S_3 is very likely by the Sb_2S_3 evaporation because we got the dark substance inside the coverer over the sample. The disappearance of Sb_2S_3 from TiO_2-NA during thermal annealing is similar to migration of CdSe from TiO_2-NA after over-annealing treatment reported in the literature.[10]

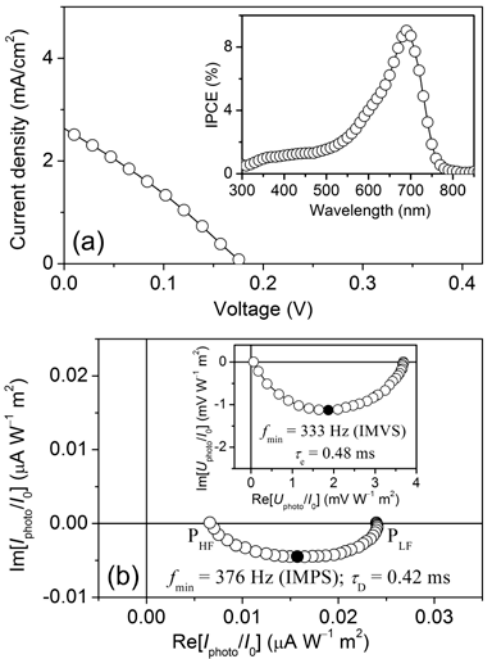

Figure S9. The *J–V* curve (a) and measured IMPS spectrum (b) of the solar cells based on the Sb_2S_3/TiO_2-BHJs crystallized at 300 °C. The insets to (a) and (b) are the IPCE and IMVS spectra of the solar cell, respectively. The solid symbol on IMPS and IMVS plots identify the f_{min} point.

Notes to Figure S9: Annealing at T_c = 300 °C results in the Sb_2S_3 in Sb_2S_3/TiO_2-BHJs not well crystallized (Figure S2) and still in nanostructured state (Figure S8). The solar cells based on the

Sb_2S_3/TiO_2-BHJs crystallized at 300 °C has a much lower J_{sc} (or J_{ph}), much smaller V_{oc}, much shorter electron lifetime τ_e (= 0.48 ms), and a much longer transit time τ_D (= 0.42 ms) (Figure S9b), as compared to the solar cells with T_c = 350 and 400 °C (Table 1 in the main text).

Interestingly, the IMPS spectrum of the solar cell based on the Sb_2S_3/TiO_2-BHJs crystallized at 300 °C locates only in the forth (IV) quadrant but not entering into III quadrant of complex plane. The measured IMPS shape of the solar cell with T_c = 300 °C is significantly different from those with T_c = 350 and 400 °C (Figure 7b in the main text) that appear dominantly in the IV quadrant of complex plane and entering into the third (III) quadrant of complex plane in high frequency regimes. The appearance of IMPS only in the IV quadrant (Figure S9b) indicates no photogenerated hole contribution to photocurrent in devices with T_c = 300 °C. Clearly, beside the difference in crystallinity and morphology in the Sb_2S_3/TiO_2-BHJs crystallized at 300 °C, the photovoltaic mechanism in the solar cell based on the Sb_2S_3/TiO_2-BHJs crystallized at 300 °C is also different from those in the Sb_2S_3/TiO_2-BHJs devices with T_c = 350 and 400 °C.

The shape of IMPS response of the solar cell with T_c = 300 °C is similar to those in the excitonic HPSCs, in which almost no photogenerated hole contribution to photocurrent exists and the lag time of charge generation behind excitation are not ignorable.[11,12] As indicated from the shape of IMPS response, we believe that the solar cell with T_c = 300 °C still takes the excitonic mechanism, with the excitons therein needing to diffuse to the Sb_2S_3/TiO_2 interface for dissociation rather than dissociate in the bulk Sb_2S_3 layer, which is similar to the cases of HPSCs[11,12] and $PbSe/TiO_2$ solar cells,[13,14] because the binding energy of the excitons in amorphous Sb_2S_3[15–17] and in nanosized Sb_2S_3[18] should be much higher due to the structural disorders than in crystalline state.

Reasonably, the solar cell with T_c = 300 °C involves the excitonic mechanism, with the exciton diffusion in Sb_2S_3 layer toward Sb_2S_3/TiO_2 interface for dissociation and no evident hole contribution to phototcurrent generation due to the very serious hole trapping by the defect states in nanostructured Sb_2S_3 layer; however, the exciton biding energy in the bulk crystalline Sb_2S_3 is very low (< 10 meV),[19] the solar cells with T_c = 350 and 400 °C take a non-excitonic mechanism in which the excitons dissociate in the bulk Sb_2S_3 layer with a remarkable hole contribution to photocurrent generation because of the formation of crystallized and continuous Sb_2S_3 layers.[20]

References

(1) Yue, W.; Wu, F.; Liu, C.; Qiu, Z.; Cui, Q.; Zhang, H.; Gao, F.; Shen, W.; Qiao, Q.; Wang, M. Incorporating $CuInS_2$ Quantum Dots into Polymer/Oxide-Nanoarray System for Efficient Hybrid Solar Cells. *Sol. Energy Mater. Sol. Cells* **2013**, 114, 43–53.

(2) Gui, E. L.; Kang, A. M.; Pramana, S. S.; Yantara, N.; Mathews, N.; Mhaisalkar, S. Effect of TiO_2 Mesoporous Layer and Surface Treatments in Determining Efficiencies in Antimony Sulfide-(Sb_2S_3) Sensitized Solar Cells. *J. Electrochem. Soc.* **2012**, *159*, B247–B250.

(3) Choi, Y. C.; Lee, D. U.; Noh, J. H.; Kim, E. K.; Seok, S. I. Highly Improved Sb_2S_3 Sensitized-Inorganic-Organic Heterojunction Solar Cells and Quantification of Traps by Deep-Level Transient Spectroscopy. *Adv. Funct. Mater.* **2014**, *24*, 3587–3592.

(4) Maiti, N.; Im, S. H.; Lim, C.-S.; Seok, S. I. A Chemical Precursor for Depositing Sb_2S_3 on to Mesoporous TiO_2 Layers in Nonaqueous Media and Its Application to Solar Cells. *Dalton Trans.* **2012**, *41*, 11569–11572.

(5) Chuang, C.-H. M.; Brown, P. R.; Bulovic, V.; Bawendi, M. G. Improved Performance and Stability in Quantum Dot Solar Cells through Band Alignment Engineering. *Nature Mater.* **2014**, *13*, 796–801.

(6) Yang, B.; Wang, L.; Han, J.; Zhou, Y.; Song, H.; Chen, S.; Zhong, J.; Lv, L.; Niu, D.; Tang, J. $CuSbS_2$ as a Promising Earth-Abundant Photovoltaic Absorber Material: A Combined Theoretical and Experimental Study. *Chem. Mater.* **2014**, *26*, 3135–3143.

(7) Boix, P. P.; Larramona, G.; Jacob, A.; Delatouche, B.; Mora-Seró, I.; Bisquert, J. Hole Transport and Recombination in All-Solid Sb_2S_3-Sensitized TiO_2 Solar Cells Using CuSCN As Hole Transporter. *J. Phys. Chem. C* **2012**,*116*, 1579–1587.

(8) Christians, J. A.; Kamat, P. V. Trap and Transfer. Two-Step Hole Injection Across the Sb_2S_3/CuSCN Interface in Solid-State Solar Cells. *ACS Nano* **2013**, *7*, 7967−7974.

(9) Christians, J. A.; Leighton, D. T., Jr.; Kamat, P. V. Rate limiting interfacial hole transfer in Sb_2S_3 solid state solar cells. *Energy Environ. Sci.* **2014**, *7*, 1148−1158.

(10) Ai, G.; Sun, W.; Gao, X.; Zhang, Y.; Peng, L.-M. Hybrid CdSe/TiO_2 nanowire photoelectrodes: Fabrication and photoelectric Performance. *J. Mater. Chem.* **2011**, *21*, 8749–8755.

(11) Chen, C.; Wang, M.; Wang, K. Characterization of Polymer/TiO_2 Photovoltaic Cells by Intensity Modulated Photocurrent Spectroscopy. *J. Phys. Chem. C* **2009**, *113*, 1624–1631.

(12) Wu, F.; Shen, W.; Cui, Q.; Bi, D.; Yue, W.; Qu, Q.; Wang, M. Dynamic Characterization of Hybrid Solar Cells Based on Polymer and Aligned ZnO Nanorods by Intensity Modulated Photocurrent Spectroscopy. *J. Phys. Chem. C* **2010**, *114*, 20225–20235.

(13) Choi, J. J; Lim, Y; Santiago-Berrios, M. B; Oh, M; Hyun, B; Sun, L; Bartnik, A. C; Goedhart, A; Malliaras, G. G; Abruña, H. D; Wise, F. W; Hanrath, T. PbSe Nanocrystal Excitonic Solar Cells. *Nano Lett.* **2009**, *9*, 3749–3755.

(14) Leschkies, K. S.; Beatty, T. J.; Kang, M. S.; Norris, D. J.; Aydil, E. S. Solar Cells Based on Junctions between Colloidal PbSe Nanocrystals and Thin ZnO Films. *ACS Nano* **2009**, *3*, 3638–3648.

(15) Evangelisti, F.; Patella, F.; Riedel, R. A.; Margaritondo, G.; Fiorini, P.; Perfetti, P.; Quaresima, C. Core Excitons in Amorphous Semiconductors. *Phys. Rev. Lett.* **1984**, *53*, 2504–2507.

(16) Gutiérrez, A.; López, M. F. First Experimental Evidence of a C-1*s* Core Exciton in Amorphous Carbon Films. *Europhys. Lett.* **1995**, *31*, 299–303.

(17) Chang, Y. K.; Hsieh, H. H.; Pong, W. F.; Tsai, M.-H.; Dann, T. E.; Chien, F. Z.; Tseng, P. K.; Chen, L. C.; Wei, S. L.; Chen, K. H.; Wu, J.-J.; Chen, Y. F. X-ray absorption of Si–C–N thin films: A comparison between crystalline and amorphous phases. *J. Appl. Phys.* **1999**, **86**, 5609–5613.

(18) Brus, L. E. Electron-Electron and Electron-Hole Interactions in Small Semiconductor Crystallites: The Size Dependence of the Lowest Excited Electronic State. *J. Chem. Phys.* **1984**, *80*, 4403–4409.

(19) Liu, C. P.; Chen, Z. H.; Wang, H. E.; Jha, S. K.; Zhang, W. J.; Bello, I.; Zapien, J. A. Enhanced Performance by Incorporation of Zinc Oxide Nanowire Array for Organic-Inorganic Hybrid Solar Cells. *Appl. Phys. Lett.* **2012**, *100*, 243102.

(20) Lin, Q.; Armin, A.; Nagiri, R. C. R.; Burn, P. L.; Meredith, P. Electro-Optics of Perovskite Solar Cells. *Nat. Photonics* **2015**, *9*, 106–112.